

# First-principles calculation of lattice thermal conductivities of $\alpha$ -, $\beta$ -, and $\gamma$ - $\text{Si}_3\text{N}_4$

Kazuyoshi Tatsumi,<sup>1,2,\*</sup> Atsushi Togo,<sup>2</sup> and Isao Tanaka<sup>2,3,4</sup>

<sup>1</sup>*Institute of Materials and Systems for Sustainability,  
Nagoya University, Chikusa, Nagoya 464-8603, Japan*

<sup>2</sup>*Center for Elements Strategy Initiative for Structural Materials,  
Kyoto University, Sakyo, Kyoto 606-8501, Japan*

<sup>3</sup>*Department of Materials Science and Engineering,  
Kyoto University, Sakyo, Kyoto 606-8501, Japan*

<sup>4</sup>*Nanostructures Research Laboratory, Japan Fine Ceramics Center, Atsuta, Nagoya 456-8587, Japan*

The lattice thermal conductivities of  $\alpha$ -,  $\beta$ - and  $\gamma$ - $\text{Si}_3\text{N}_4$  phases are investigated from *ab-initio* anharmonic lattice dynamics, within the single-mode relaxation-time approximation of the linearized phonon Boltzmann transport equation. At 300 K, the lattice thermal conductivity of  $\beta$ - $\text{Si}_3\text{N}_4$  is calculated as  $\kappa_{xx} = 73$  and  $\kappa_{zz} = 199$  (in units of  $\text{W m}^{-1} \text{K}^{-1}$ ), which is consistent with the reported experimental values of 69 and 180, respectively. For  $\alpha$ - $\text{Si}_3\text{N}_4$ ,  $\kappa_{xx} = 68$  and  $\kappa_{zz} = 100$  are obtained. The difference in anisotropy between these phases originates from the characteristic differences in their phonon band structures, which is closely related to the crystal structures. In  $\alpha$ - $\text{Si}_3\text{N}_4$ , acoustic-mode phonons below 6 THz are the main heat carriers, while in  $\beta$ - $\text{Si}_3\text{N}_4$ , the phonon modes up to 12 THz contribute to the lattice thermal conductivity. In  $\gamma$ - $\text{Si}_3\text{N}_4$ ,  $\kappa = 77$  is obtained. The distribution of phonon mode contributions to the lattice thermal conductivity with respect to phonon frequency closely resembles that for  $\kappa_{xx}$  of  $\beta$ - $\text{Si}_3\text{N}_4$ , although the phonon lifetimes for  $\gamma$ - $\text{Si}_3\text{N}_4$  are half as short as those for  $\beta$ - $\text{Si}_3\text{N}_4$ .

## I. INTRODUCTION

Several nitride insulators are known to exhibit high thermal conductivity, which is important for heat transfer materials at elevated temperatures. For example, Slack *et al.*<sup>1</sup> reported that wurtzite-type AlN has thermal conductivity that exceeds  $100 \text{ W m}^{-1} \text{K}^{-1}$ .  $\text{Si}_3\text{N}_4$  has become another promising thermal conductive insulator because its thermal conductivity has been improved up to  $177 \text{ W m}^{-1} \text{K}^{-1}$  through the use of advanced ceramic technologies related to densification and microstructure control.<sup>2-5</sup> The  $\text{Si}_3\text{N}_4$  ceramics also exhibit high mechanical strength at elevated temperatures; therefore, they are regarded as ideal materials for use in various applications, such as engine components, gas turbines, and heat sink substrates of power semiconductor devices.

At atmospheric pressure,  $\text{Si}_3\text{N}_4$  has two phases,  $\alpha$  and  $\beta$ , which are generally considered as low- and high-temperature phases, respectively.<sup>2,6,7</sup> Their crystal structures belong to the  $P31c$  and  $P6_3/m$  space groups, respectively.<sup>8,9</sup> These structures have different manners of stacking equivalent basal layer structures composed of  $\text{SiN}_4$  tetrahedra.<sup>10</sup> Fig. 1 depicts these layer structures from the principal axis direction. They are denoted as A, B, C, and D in the  $\alpha$  phase, and A and B in the  $\beta$  phase. The stacking manners are thus ABCDABCD... and ABAB..., respectively. The  $\alpha$  phase has additional two layer structures of C and D, which are related to A and B by the  $c$  glide operation.<sup>10</sup> Along this direction, the lattice constant of the  $\alpha$  phase is approximately twice as long as that of the  $\beta$  phase.

The experimental thermal conductivities<sup>2-5,12</sup> of the  $\text{Si}_3\text{N}_4$  polymorphs were measured for bulk polycrystalline samples. These values were significantly affected by the lattice defects, impurities, shapes and orientations of the

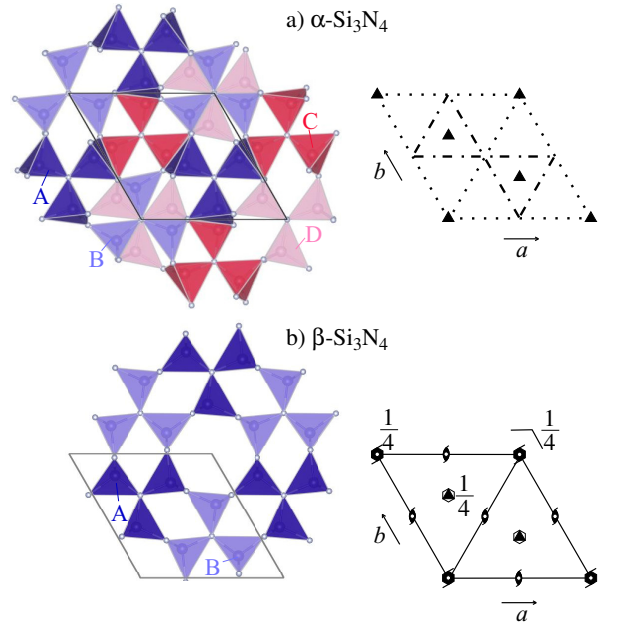


FIG. 1. (color online) Crystal structures of  $\alpha$ - and  $\beta$ - $\text{Si}_3\text{N}_4$ . Stacking of  $\text{SiN}_4$  tetrahedron layers are shown at the left. (a) ABCDABCD... for  $\alpha$ - $\text{Si}_3\text{N}_4$ . (b) ABAB... for  $\beta$ - $\text{Si}_3\text{N}_4$ . Space group diagrams<sup>11</sup> for  $P31c$  ( $\alpha$ - $\text{Si}_3\text{N}_4$ ) and  $P6_3/m$  ( $\beta$ - $\text{Si}_3\text{N}_4$ ) are shown at the right.

constituent crystal grains;<sup>6</sup> the intrinsic thermal conductivity of defect-free  $\text{Si}_3\text{N}_4$  has not been established. As an experimental approach to determine this, Li *et al.*<sup>13</sup> applied the high-resolution thermoreflectance microscopy to single  $\beta$ - $\text{Si}_3\text{N}_4$  grains in a ceramic sample. The thermal conductivity was analyzed as 69 and  $180 \text{ W m}^{-1} \text{K}^{-1}$  along the  $a$  and  $c$  axes, respectively. These val-

ues respectively correspond to the  $xx$  and  $zz$  elements of the lattice thermal conductivity tensor,  $\kappa$ . We consider the anisotropy of  $\kappa_{zz}/\kappa_{xx} \sim 3$  is relatively large. Hirotsaki *et al.*<sup>6</sup> theoretically estimated  $\kappa$  by application of the Green-Kubo formulation to the molecular dynamics (MD) method with the interatomic potentials proposed by Vashishta *et al.*<sup>14</sup>. They calculated  $\kappa_{xx}$  and  $\kappa_{zz}$  of  $\alpha$ -Si<sub>3</sub>N<sub>4</sub> to be 105 and 225 W m<sup>-1</sup> K<sup>-1</sup>, and those of  $\beta$ -Si<sub>3</sub>N<sub>4</sub> as 170 and 450 W m<sup>-1</sup> K<sup>-1</sup>, respectively. The ratio  $\kappa_{zz}/\kappa_{xx}$  in  $\beta$ -Si<sub>3</sub>N<sub>4</sub> agreed well with the experimental ratio;  $\kappa_{xx}$  and  $\kappa_{zz}$  were overestimated by more than two times those of the corresponding experimental  $\kappa$  values.

Based on first principles calculations and Boltzmann transport theory<sup>15</sup>, Togo *et al.* recently calculated  $\kappa$  of many polymorphs of the zincblende- and wurtzite-type structures. Their crystal structures have stacking manners of the densest atom planes as ABCABC... and ABAB..., respectively. The different stacking manners merely altered  $\kappa$ , the phonon linewidths and the phonon density of states (DOS).<sup>15</sup> On the other hand, the previous MD results indicated that the different stacking manners between the  $\alpha$  and  $\beta$  phases altered  $\kappa$  significantly. This has not been explained with respect to their phonon properties. Therefore, it is of interest to investigate this based on the first principles anharmonic phonon calculation.

In addition to the  $\alpha$  and  $\beta$  phases, a cubic spinel phase ( $\gamma$ -Si<sub>3</sub>N<sub>4</sub>) is known to form upon compression and *in situ* heating.<sup>16,17</sup> The reported transition pressures are scattered from 10 to 36 GPa, depending on the experimental conditions.<sup>18</sup> The  $\gamma$  phase is experimentally quenched to atmospheric pressure and room temperature. The thermal conductivity of the  $\gamma$  phase has not been experimentally reported, although it has been estimated by the Slack model.<sup>19</sup>

The present study aims to qualitatively elucidate the lattice thermal conductivity tensors among the three Si<sub>3</sub>N<sub>4</sub> phases by a first principles approach. We calculate  $\kappa$  of the  $\gamma$  phase as well, for systematic understanding. After the methodology is described, we examine the validity of the present results; through comparison of the calculated thermal properties with the available experimental and theoretical references. The characteristic behaviors of  $\kappa$  are then investigated in detail on the basis of the phonon band structures and phonon lifetimes.

## II. COMPUTATIONAL PROCEDURES

### A. Lattice thermal conductivity calculation

The lattice thermal conductivities were calculated by solving the linearized Boltzmann transport equation (LBTE) within the single-mode relaxation time approximation (single-mode RTA). The harmonic phonon states and lattice thermal conductivities were calculated with the phonopy<sup>20</sup> and phono3py<sup>15</sup> software packages, re-

spectively. We also attempted the direct-solution of LBTE<sup>21</sup> and give the calculated  $\kappa$  values in the following section. The difference between  $\kappa$  calculated by the single-mode RTA and that by the direct solution was minor for our discussion, for which the detail is given in Sec. IIc. Therefore, this research was limited to use the single-mode RTA to take advantage of the closed form of  $\kappa$ , which can be intuitively understood in terms of mode-specific phonon properties.

In the following sections, we denote the phonon mode by  $\lambda = (\mathbf{q}, p)$  with the set of the phonon wave vector  $\mathbf{q}$  and band index  $p$  and  $-\lambda \equiv (-\mathbf{q}, p)$ . The harmonic phonon frequency of the phonon mode  $\lambda$  is denoted by  $\omega_\lambda$ . The relaxation time due to phonon-phonon scattering was obtained as,  $\tau_{\lambda, \text{ph-ph}} = [2\Gamma_\lambda(\omega_\lambda)]^{-1}$ , with

$$\Gamma_\lambda(\omega) = \frac{18\pi}{\hbar^2} \sum_{\lambda'\lambda''} |\Phi_{-\lambda\lambda'\lambda''}|^2 N_2(\mathbf{q}, \omega). \quad (1)$$

In this equation,  $\hbar$  is the reduced Planck constant and  $\Phi_{\lambda\lambda'\lambda''}$  denotes the three-phonon-scattering strength, obtained by the usual coordinate transformation of third-order force constants from direct space to phonon space.<sup>15</sup> The second- and third-order real-space force constants were obtained by *ab initio* calculation, of which the details are given in the next section.  $N_2(\mathbf{q}, \omega)$  is a weighted joint DOS (WJDOS)<sup>15</sup>,

$$N_2(\mathbf{q}, \omega) = N_2^{(1)}(\mathbf{q}, \omega) + N_2^{(2)}(\mathbf{q}, \omega) \quad (2)$$

where

$$\begin{aligned} N_2^{(1)} &= \frac{1}{N_{\mathbf{q}}} \sum_{\lambda'\lambda''} (n_{\lambda'} - n_{\lambda''}) \Delta(-\mathbf{q} + \mathbf{q}' + \mathbf{q}'') \\ &\times [\delta(\omega + \omega_{\lambda'} - \omega_{\lambda''}) - \delta(\omega - \omega_{\lambda'} + \omega_{\lambda''})], \\ N_2^{(2)} &= \frac{1}{N_{\mathbf{q}}} \sum_{\lambda'\lambda''} (n_{\lambda'} + n_{\lambda''} + 1) \Delta(-\mathbf{q} + \mathbf{q}' + \mathbf{q}'') \\ &\times \delta(\omega - \omega_{\lambda'} - \omega_{\lambda''}), \end{aligned}$$

with  $\Delta(\mathbf{x})$  giving 1 if  $\mathbf{x}$  is a reciprocal lattice vector, and otherwise zero. This constraint comes from the lattice translational invariance that appears inside  $\Phi_{\lambda\lambda'\lambda''}$ ,<sup>15</sup> however, we let it appear in  $N_2$  in Eq. (1) for the analysis given below.  $N_{\mathbf{q}}$  is the number of  $\mathbf{q}$ -points. The weighting terms are composed of  $n_\lambda = [\exp(\hbar\omega_\lambda/k_B T) - 1]^{-1}$ , the Bose-Einstein distribution at temperature  $T$  with  $k_B$  of Boltzmann constant.

To more realistically compare the calculated  $\kappa$  with the measured thermal conductivities, the isotopic scattering effect due to the natural isotope distribution was taken into account according to the second-order perturbation theory.<sup>22</sup> Using the relaxation times for the phonon-phonon scattering and isotopic scattering,  $\tau_{\lambda, \text{ph-ph}}$  and  $\tau_{\lambda, \text{iso}}$ , respectively, the total relaxation time for a phonon mode,  $\tau_\lambda$ , was calculated by assuming Matthiessen's rule,  $1/\tau_\lambda = 1/\tau_{\lambda, \text{ph-ph}} + 1/\tau_{\lambda, \text{iso}}$ .

The closed form of  $\kappa$  within the RTA was obtained via

$$\kappa = \frac{1}{N_{\mathbf{q}}\Omega} \sum_{\lambda} \tau_\lambda \mathbf{v}_\lambda \otimes \mathbf{v}_\lambda c_\lambda, \quad (3)$$

where  $\Omega$  is the unit cell volume,  $\mathbf{v}_\lambda = \nabla_{\mathbf{q}}\omega_\lambda$  is the group velocity, and  $c_\lambda = \frac{\partial(n_\lambda\hbar\omega_\lambda)}{\partial T}$  is the mode heat capacity. To analyze  $\kappa$  in detail, the cumulative thermal conductivity:

$$\kappa^c(\omega) = \frac{1}{N_{\mathbf{q}}\Omega} \int_0^\omega \sum_\lambda \tau_\lambda \mathbf{v}_\lambda \otimes \mathbf{v}_\lambda c_\lambda \delta(\omega' - \omega_\lambda) d\omega', \quad (4)$$

and its derivative  $\frac{d\kappa^c(\omega)}{d\omega}$ :

$$\frac{d\kappa^c(\omega)}{d\omega} = \frac{1}{N_{\mathbf{q}}\Omega} \sum_\lambda \tau_\lambda \mathbf{v}_\lambda \otimes \mathbf{v}_\lambda c_\lambda \delta(\omega - \omega_\lambda), \quad (5)$$

were calculated to determine the phonon mode contributions to  $\kappa$ .

## B. Computational details

The force constants required were calculated using the first-principles projector augmented wave method<sup>23</sup> (VASP code<sup>24-26</sup>). The generalized gradient approximation (GGA) parameterized by Perdew, Burke, and Ernzerhof<sup>27</sup> was used for the exchange correlation potential. A plane wave energy cutoff of 500 eV was employed. The crystal structures were optimized for 0 K and 0 GPa until the residual forces acting on the constituent atoms were less than  $10^{-6}$  eV  $\text{\AA}^{-1}$ . Here, the temperature and pressure were considered only for the electronic system and the zero point lattice vibration was not considered. The calculated lattice parameters were  $a = 7.808$   $\text{\AA}$  and  $c = 5.659$   $\text{\AA}$  for the  $\alpha$  phase,  $a = 7.660$   $\text{\AA}$  and  $c = 2.925$   $\text{\AA}$  for the  $\beta$  phase, and  $a = 7.787$   $\text{\AA}$  for the  $\gamma$  phase, which are in agreement with the experimental data<sup>8,9,28</sup> within +0.7 % error. The lattice volume optimized with the local density approximation (LDA)<sup>29</sup> for the exchange correlation potential was, for  $\beta$ -Si<sub>3</sub>N<sub>4</sub>, 3 % smaller than the volume optimized with GGA, which is a typical volume contraction of LDA.  $\kappa_{xx}$  and  $\kappa_{zz}$  calculated with LDA were larger by 0.3 and 2.6 % than those calculated with GGA. For our discussion, these differences are sufficiently small; therefore, the impact of the choice of exchange correlation potential is considered to be minor in this study.

The force constants were calculated by the finite difference approach<sup>30</sup>. For this calculation, the following supercells were adopted:  $1 \times 1 \times 2$ ,  $1 \times 1 \times 3$ , and  $1 \times 1 \times 1$  supercells of the conventional unit cells for the calculations of the third-order force constants of  $\alpha$ ,  $\beta$ , and  $\gamma$ -Si<sub>3</sub>N<sub>4</sub>, respectively, and  $3 \times 3 \times 4$ ,  $3 \times 3 \times 8$  and  $2 \times 2 \times 2$  for those of the second-order force constants. The length of the induced atomic displacements was set to 0.03  $\text{\AA}$ . Table I shows  $\kappa$  calculated with several different sets of the supercells, which indicates that the calculated  $\kappa$  has reasonable convergence with respect to the size of the supercells.

Uniform  $\mathbf{k}$ -point sampling meshes of  $4 \times 4 \times 2$ ,  $4 \times 4 \times 3$ , and  $3 \times 3 \times 3$  were employed for calculations of the third-order force constants of the  $\alpha$ ,  $\beta$ , and  $\gamma$  phases. For

TABLE I. Calculated lattice thermal conductivities of  $\alpha$ -,  $\beta$ -, and  $\gamma$ -Si<sub>3</sub>N<sub>4</sub> (W K<sup>-1</sup> m<sup>-1</sup>) at 300 K with respect to several combinations of supercell sizes.

Phase	Supercell (# of atoms)		LTC	
	3 <sup>rd</sup> force constants	2 <sup>nd</sup> force constants	$xx$	$zz$
$\alpha$	$1 \times 1 \times 1$ (28)	$1 \times 1 \times 1$ (28)	37	57
	$1 \times 1 \times 2$ (56)	$1 \times 1 \times 2$ (56)	41	79
	$1 \times 1 \times 1$ (28)	$2 \times 2 \times 2$ (224)	55	81
	$1 \times 1 \times 2$ (56)	$2 \times 2 \times 2$ (224)	67	95
	$1 \times 1 \times 2$ (56)	$2 \times 2 \times 3$ (336)	68	97
	$1 \times 1 \times 2$ (56)	$3 \times 3 \times 4$ (1008)	68	100
$\beta$	$1 \times 1 \times 2$ (28)	$1 \times 1 \times 2$ (28)	44	173
	$1 \times 1 \times 2$ (28)	$2 \times 2 \times 4$ (224)	76	208
	$1 \times 1 \times 3$ (42)	$2 \times 2 \times 4$ (224)	71	194
	$1 \times 1 \times 3$ (42)	$2 \times 2 \times 5$ (280)	72	196
	$1 \times 1 \times 3$ (42)	$3 \times 3 \times 8$ (1008)	73	199
$\gamma$	$1 \times 1 \times 1$ (56)	$1 \times 1 \times 1$ (56)	72	
	$1 \times 1 \times 1$ (56)	$2 \times 2 \times 2$ (448)	77	
	$1 \times 1 \times 1$ (56)	$3 \times 3 \times 3$ (56)	79	

the  $\alpha$  and  $\beta$  phases, the center of the  $a^*b^*$  plane was sampled, while the center on the  $c^*$ -axis was not. For the  $\gamma$  phase, a non- $\Gamma$  center mesh was used. For the calculations of the second-order force constants, the  $\Gamma$ -point was only sampled for the  $\alpha$  and  $\beta$  phases, and the only one  $\mathbf{k} = (0.5, 0.5, 0.5)$  point was sampled for the  $\gamma$  phase. The  $\mathbf{q}$ -point sampling meshes of  $10 \times 10 \times 14$ ,  $10 \times 10 \times 26$ , and  $12 \times 12 \times 12$  were employed to calculate  $\kappa$  in Eq. (3) for the  $\alpha$ ,  $\beta$ , and  $\gamma$  phases, respectively.

Non-analytical term correction<sup>31</sup> was applied to the second-order force constants to take into account the long range coulombic forces present in ionic crystals. For the correction, static dielectric constants and Born effective charges were calculated using the density functional perturbation theory as implemented in the VASP code<sup>32,33</sup>.

The effect of lattice thermal expansion on  $\kappa$  was examined by the calculation of  $\kappa$  for several finite temperatures with the crystal structures optimized for the corresponding temperatures within the quasi-harmonic approximation (QHA)<sup>34</sup>. These  $\kappa$  were different from those calculated for the same temperatures with the structure optimized for 0 K. We consider these differences as the effect of lattice thermal expansion. The differences in  $\kappa$  for  $T=300, 600, 900, 1200$ , and,  $1500$  K, for the  $\beta$  phase, were within 1 %. They were similar to those for Si and Ge calculated by Ward *et al.*<sup>35</sup>. For the present study, these differences are negligible and for finite temperatures  $\kappa$  calculated with the structure optimized for 0 K was adopted.

The volumetric thermal expansion coefficients were also calculated. Comparison with the experimental coefficient is useful to validate the present thermal conductivity calculation because both the thermal expansion and  $\kappa$  originate from the anharmonicity of the interatomic

potential. The calculated coefficients of the  $\alpha$ ,  $\beta$ , and  $\gamma$  phases were  $4.31 \times 10^{-6}$ ,  $4.19 \times 10^{-6}$ , and  $1.13 \times 10^{-5}$   $\text{K}^{-1}$  for 300 K, while the experimental values<sup>36,37</sup> were  $3.75 \times 10^{-6}$ ,  $3.55 \times 10^{-6}$ , and  $9.48 \times 10^{-6}$   $\text{K}^{-1}$ . The calculation systematically overestimated the experimental values, but reproduced the experimental tendencies, including that the  $\alpha$  phase has a slightly larger thermal expansion coefficient than the  $\beta$  phase. This supports the validity of the present calculation to qualitatively compare the calculated  $\kappa$  among the  $\text{Si}_3\text{N}_4$  phases.

To compare the microscopic phonon properties among the three phases under the same conditions, the results calculated at 0 GPa are shown and discussed. For the  $\gamma$  phase, this means that we assume the condition of a virtually quenched  $\gamma$  phase at 0 GPa from the high pressure. To examine the analytical continuity of the properties with respect to pressure,  $\kappa$  of the  $\gamma$  phase was calculated at 10, 20, and 40 GPa, as shown in Fig. 7. The phenomenological behavior of the linear dependence of  $\kappa$  with respect to the pressure was reproduced, similar to that in Ref. 38. The slope was  $2.89 \text{ W m}^{-1} \text{ K}^{-1} \text{ GPa}^{-1}$  for the  $\gamma$  phase. From this dependence, we consider that the microscopic values are also varied smoothly with the pressure and those at 0 GPa are valuable for comparison with the corresponding values of the  $\alpha$  and  $\beta$  phases.

### C. Direct solution of LBTE

The advantage of employing the single-mode RTA for thermal conductivity calculations is the closed form Eq. (3), by which the qualitative character of  $\kappa$  can be intuitively understood in terms of the phonon-mode specific properties. The microscopic understanding of the full solution of LBTE is still under development,<sup>39</sup> and the microscopic picture based on collective phonons<sup>40</sup> will require more complicated investigation.

Single-mode RTA solutions of LBTE often underestimate the full solution.<sup>35,41</sup> To check this underestimation,  $\kappa$  for the  $\alpha$  and  $\beta$  phases were calculated by the direct solution of LBTE<sup>21</sup>, which is one of the methods of LBTE full solutions.  $\kappa_{xx}$  and  $\kappa_{zz}$  without the isotope effect were 69 and 102  $\text{W m}^{-1} \text{ K}^{-1}$  for the  $\alpha$  phase, and 76 and 238  $\text{W m}^{-1} \text{ K}^{-1}$  for the  $\beta$  phase, respectively, while the corresponding single-mode RTA values were 70 and 102  $\text{W m}^{-1} \text{ K}^{-1}$  for the  $\alpha$  phase, and 76 and 210  $\text{W m}^{-1} \text{ K}^{-1}$  for the  $\beta$  phase.  $\kappa_{zz}$  for the  $\beta$  phase from the direct solution was 13 % larger than that of the single-mode RTA solution. The differences in  $\kappa$  between the LBTE solutions are not significant; therefore, we expect that the physics of these lattice thermal conductivities is well understood within the single-mode RTA at the current level of our interest. Therefore, we discuss the lattice thermal conductivities calculated by the single-mode RTA solution.

## III. RESULTS AND DISCUSSION

### A. Lattice thermal conductivities

TABLE II. Calculated thermal conductivities of  $\alpha$ - $\text{Si}_3\text{N}_4$  (trigonal),  $\beta$ - $\text{Si}_3\text{N}_4$  (trigonal), and  $\gamma$ - $\text{Si}_3\text{N}_4$  (cubic) at 300 K in units of  $\text{W m}^{-1} \text{ K}^{-1}$ , compared with the experimental and theoretical reference data. Theoretical bulk moduli  $B$  (in units of GPa), calculated from the elastic constant calculation routine<sup>42</sup> in the VASP code.

	This work			$\kappa$	Ref. Theo.		Ref. Expt.	
	$\kappa_{xx}$	$\kappa_{zz}$	$B$		$\kappa_{xx}$	$\kappa_{zz}$	$\kappa_{xx}$	$\kappa_{zz}$
$\alpha$ - $\text{Si}_3\text{N}_4$	68	100	224	70 <sup>a</sup>	105 <sup>b</sup>	225 <sup>b</sup>	-	-
$\beta$ - $\text{Si}_3\text{N}_4$	73	199	237	250 <sup>a</sup>	170 <sup>b</sup>	450 <sup>b</sup>	69 <sup>c</sup>	180 <sup>c</sup>
$\gamma$ - $\text{Si}_3\text{N}_4$	77	-	296	80 <sup>a</sup>	-	-	-	-

<sup>a</sup> Ref. 19, Slack model.

<sup>b</sup> Ref. 6, molecular dynamics (Green-Kubo).

<sup>c</sup> Ref. 13, single crystalline grains of poly-crystals.

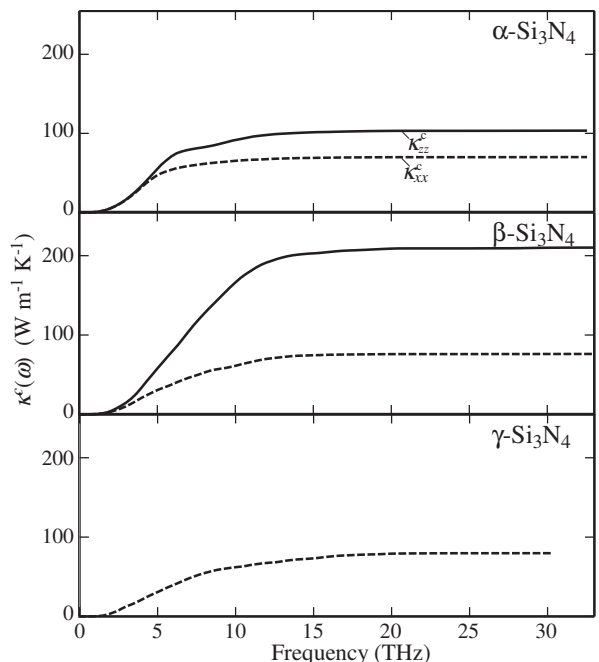


FIG. 2. Cumulative thermal conductivity of the three phases.

Table II shows the calculated  $\kappa$  for 300 K with the isotope effect.  $\beta$ - $\text{Si}_3\text{N}_4$  has a markedly more anisotropic  $\kappa$  than  $\alpha$ - $\text{Si}_3\text{N}_4$ . The directional averages  $\sum_i \kappa_{ii}/3$  are 79, 115, and 77  $\text{W m}^{-1} \text{ K}^{-1}$  for the  $\alpha$ ,  $\beta$ , and  $\gamma$  phases, respectively. The value for the  $\gamma$  phase is similar to that for the  $\alpha$  phase, despite the comparatively large difference among the bulk moduli ( $B$ ) that are also shown in Table II.

Table II also lists the previously reported experimental<sup>13</sup> and theoretical<sup>6</sup>  $\kappa$  for reference. The

theoretical results<sup>19</sup> of the Slack model, which do not include the anisotropy in  $\kappa$ , are shown as  $\kappa$  in Table II. Compared to the  $\kappa$  from MD<sup>6</sup>, our  $\kappa$  for the  $\beta$  phase has better agreement with the experimental  $\kappa$ . Compared to  $\kappa$  from the Slack model, our directional average  $\sum_i \kappa_{ii}/3$  is also much closer to the experimental average.

Fig. 2 shows the cumulative thermal conductivity,  $\kappa^c(\omega)$ . From this figure, it is evident that in the  $\alpha$ ,  $\beta$ , and  $\gamma$  phases, the phonon modes with their frequencies up to  $\sim 6$ , 12 and 10 THz largely contribute to each respective  $\kappa$ .

### B. Distribution of group velocity in Brillouin zone

The Brillouin zones and phonon band diagrams of the three phases are shown in Fig.3-a. In this figure, we investigate the frequency gradients, the group velocities projected on the paths along the nonequivalent axes of the reciprocal lattice. We particularly focus on the anisotropy of the group velocities in the  $\alpha$  and  $\beta$  phases. This was not investigated in the previous works. The band diagrams on the other high-symmetry paths are almost identical to those reported<sup>18,43</sup> and thus are not shown. For the  $\alpha$  and  $\beta$  phases, in order to investigate the behaviors of the group velocities at the other  $\mathbf{q}$  points, the cross-section of the phonon frequency distribution on the  $b^*c^*$  plane is shown in Fig.3-c. Since the cross-section on the other planes containing the  $c^*$  axis did not differ much from that shown in Fig.3-c, we focus on the  $b^*c^*$  plane as a representative of all such planes. We show only the frequencies of the four modes from the lowest frequency, #1, 2, 3, and 4, because they contribute significantly to  $\kappa$ . The paths of the band diagrams correspond to the edges in the bottom and left sides of the cross-sections. The dispersion curves on these edges for the cross-section of #4 are denoted by a thick gray line in Fig.3-b, so as to connect the dispersion curves with the cross-sections.

In the band diagram of the  $\alpha$  phase, the dispersion curves of the acoustic phonon modes are not much different between the cases for the  $\Gamma$ -A and  $\Gamma$ -K paths, indicating the isotropic group velocities of the acoustic phonons. The contour maps including the most of the acoustic phonon modes are #1, 2, and 3 in Fig.3-c. For the  $\alpha$  phase, these maps clearly show the isotropic group velocities: The most of the iso-frequency lines in the contours are parallel to the circular dash lines inserted as a guide. In contrast, in the band diagram of the  $\beta$  phase, the acoustic phonon modes show much higher  $\omega_\lambda$  at the A point than at the K point. In the contour maps of #1, 2, and 3 for the  $\beta$  phase, the gradients of  $\omega_\lambda$  are, in the most part, parallel to the  $\Gamma$ -A path; the group velocities orient to the  $c^*$  axis direction.

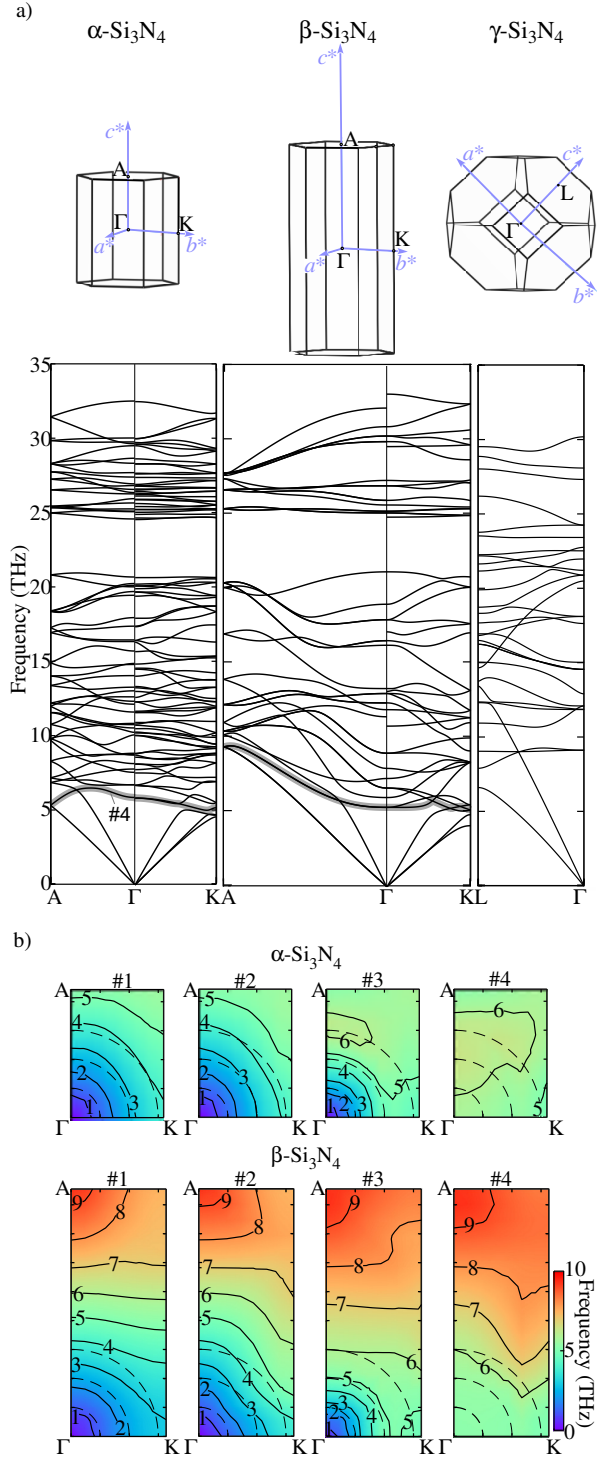


FIG. 3. (color online) (a,b) Brillouin-zones and band diagrams of the three phases. (c) Contour maps of phonon frequencies for the  $\alpha$  and  $\beta$  phases, on the  $b^*c^*$  planes of Brillouin-zones. The maps for the four lowest-frequency phonon modes (#1, 2, 3, and 4) are shown. In the band diagrams, the dispersion curve of #4 is denoted by a thick gray line.

This difference between the  $\alpha$  and  $\beta$  phases is due to the



$\Gamma$ -A path lengths. The  $\beta$  phase has an approximately twice longer path than the  $\alpha$  phase; the lattice constant  $c$  of the  $\beta$  phase is nearly half that of the  $\alpha$  phase, owing to the different stacking manners of the basal layer structures (Fig.1). Comparing the contour maps of #4 for  $\alpha$  and  $\beta$  phases, there is a tendency that  $\beta$  phase has larger group velocities than  $\alpha$  phase. Comparing the band diagrams of the  $\alpha$  and  $\beta$  phases, the same tendency is seen for the most branches of the optical phonon modes  $\lesssim 10$  THz, where the phonon modes largely contribute to  $\kappa$ .

In the  $\gamma$  phase, the dispersion curve of the longitudinal acoustic phonon modes is almost linear. Their frequencies near the L point is much higher than the longitudinal acoustic phonon frequencies near the A or K points of the  $\alpha$  and  $\beta$  phases. The gradients of the dispersion curve are largest among the three phases, as expected by the largest  $B$ .

### C. Frequency distributions of phonon properties

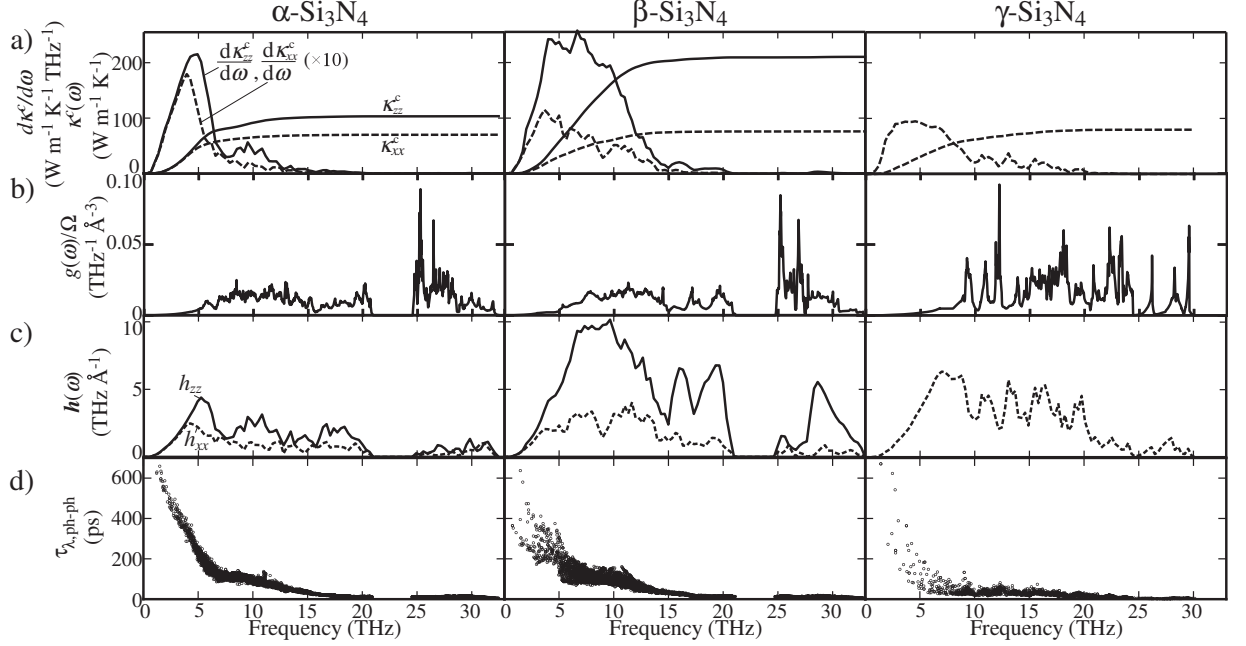


FIG. 4. Microscopic phonon properties of three  $\text{Si}_3\text{N}_4$  phases. (a) Cumulative thermal conductivity  $\kappa^c$  and its frequency derivative, (b) DOS as  $g(\omega)$ , (c) DOS weighted with  $\mathbf{v}_\lambda \otimes \mathbf{v}_\lambda$  as  $\mathbf{h}(\omega)$ , and (d) scatter plots of phonon lifetimes and phonon frequencies,  $(\tau_\lambda, \omega_\lambda)$ .

In the previous two sections, we have investigated the anisotropy in  $\mathbf{v}_\lambda$ , which may explain the anisotropy in  $\kappa$ . Here we examine which phonon frequencies and which terms in Eq.(3) characterize the behavior of the calculated  $\kappa$ . In the following, we omit the term of mode heat capacity because it is approximately constant for the phonon modes that mainly carry heat at 300 K. For simplicity, the effect of isotope scattering is not considered in this section. For the investigation, the cumulative thermal conductivity,  $\kappa^c(\omega)$  in Eq.(5), and its derivative  $d\kappa^c/d\omega$ , are shown at the top of Fig. 4. From this figure, it is evident that in the  $\alpha$ ,  $\beta$ , and  $\gamma$  phases, the phonon modes with their frequencies up to  $\sim 6$ , 12, and 10 THz largely contribute to each respective  $\kappa$ . The frequencies shown in the contour maps in Fig. ?? are within these frequency ranges, and thus it is confirmed that these bands make a significant contribution to  $\kappa$ .

Assuming that  $\tau_\lambda$  and  $\mathbf{v}_\lambda$  are constant, then  $d\kappa_{ii}^c/d\omega$

( $ii=xx, zz$ ) are proportional to the phonon DOS:

$$g(\omega) = \frac{1}{N_{\mathbf{q}}} \sum_{\lambda} \delta(\omega - \omega_{\lambda}). \quad (6)$$

We refer to  $g(\omega)/\Omega$  as frequency distributions of heat carrier density. Alternatively, assuming that only  $\tau_\lambda$  is constant, then  $d\kappa^c/d\omega$  is proportional to:

$$\mathbf{h}(\omega) = \frac{1}{N_{\mathbf{q}}\Omega} \sum_{\lambda} \mathbf{v}_\lambda \otimes \mathbf{v}_\lambda \delta(\omega - \omega_{\lambda}), \quad (7)$$

from which we examine the impacts of both of  $\mathbf{v}_\lambda$  and the heat carrier density.  $g(\omega)/\Omega$  and  $\mathbf{h}(\omega)$  are shown in Figs. 4(b) and (c). As for the frequency variation of  $\tau_{\lambda, \text{ph-ph}}$ , the phonon lifetimes are shown as scatter plots of  $(\tau_{\lambda, \text{ph-ph}}, \omega_\lambda)$  in Fig. 4(d).

Comparison of the  $\alpha$  and  $\beta$  phases indicates their phonon lifetimes distributions are qualitatively similar, except for a striking difference below  $\sim 5$  THz, which

will be examined later. The markedly different  $d\kappa_{ii}^c/d\omega$  between the two phases are therefore ascribed to the corresponding  $h_{ii}$ . The overall spectral shapes of  $g(\omega)/\Omega$  are also similar between the two phases; therefore,  $\mathbf{v}_\lambda$  alone accounts for the different behavior of  $d\kappa_{ii}^c/d\omega$ . It is thus concluded that the different anisotropy in  $\kappa$  can be qualitatively explained by the different  $\mathbf{v}_\lambda$ . In contrast, for the zincblende and wurtzite structures, the group velocities are suggested to be similar from their band structures<sup>15</sup>. This must result in similar  $\kappa$  between these structures, irrespective of the stacking manner.

The  $\gamma$  phase has much different  $g(\omega)/\Omega$ ,  $\mathbf{h}(\omega)$ , and,  $\tau_{\lambda,\text{ph-ph}}$  from the other phases, as expected from the large differences in their crystal structures. The most significant difference is in the phonon lifetimes. For 4 THz  $\lesssim \omega_\lambda \lesssim 10$  THz, the phonon lifetimes are approximately half as short as those of the other phases. We will examine this in detail later. As a result,  $d\kappa_{xx}^c/d\omega$  has relatively low intensities. The longitudinal acoustic phonon branch increases its frequencies much significantly, as we have examined in the band diagram; therefore,  $d\kappa_{xx}^c/d\omega$  rather gradually attenuates as the frequency increases, occasionally resembling  $d\kappa_{xx}^c/d\omega$  of the  $\beta$  phase.

The distribution of phonon lifetimes is qualitatively similar between the  $\alpha$  and  $\beta$  phases, although their group velocities have marked differences. This remains a curiosity. Analogous to the report by Lindsay *et al.*<sup>44</sup>, we can say that  $\tau_{\lambda,\text{ph-ph}}$  in the present form is dependent on the phase space for the available two phonons,  $\{\lambda', \lambda''\}$ , and is also dependent on  $|\Phi_{\lambda\lambda'\lambda''}|^2$ . We examine these terms one-by-one. A distribution of two-phonon configurations satisfying the energy and momentum conservation law is represented as WJDOS<sup>15</sup>.

The frequency profiles of WJDOS in Fig. 5 are very similar between the  $\alpha$  and  $\beta$  phases, for each different  $\mathbf{q}$ -points. Their intensities are scaled with  $Z^2$  of which  $Z$  is the number of formula units in the primitive unit cell, to compare WJDOS for structures with different  $Z$ . These profiles show weak  $\mathbf{q}$ -point dependences. The frequency profile for the  $\gamma$  phase is only shown at  $\mathbf{q} = (0, 0, 0)$  because of the different shape of the Brillouin zone from those in the other phases. We checked that the  $\mathbf{q}$  dependence of WJDOS for the  $\gamma$  phase was as weak as those shown in Fig. 5 for the  $\alpha$  and  $\beta$  phases. The intensities of WJDOS below  $\sim 10$  THz in the  $\gamma$  phase are slightly smaller than those in the other phases.

TABLE III. Averages of  $|\Phi_{\lambda\lambda'\lambda''}|^2$  over frequency ranges of  $\omega_\lambda$  (0–15 and 0–35 THz) and all  $(\lambda', \lambda')$ . The values are in units of  $\text{meV}^2$ .

Frequency range (THz)	Phase		
	$\alpha$	$\beta$	$\gamma$
0–15	0.47	0.46	1.02
0–35	2.30	2.30	2.02

As for  $|\Phi_{\lambda\lambda'\lambda''}|^2$ , in Table. III, they are averaged over

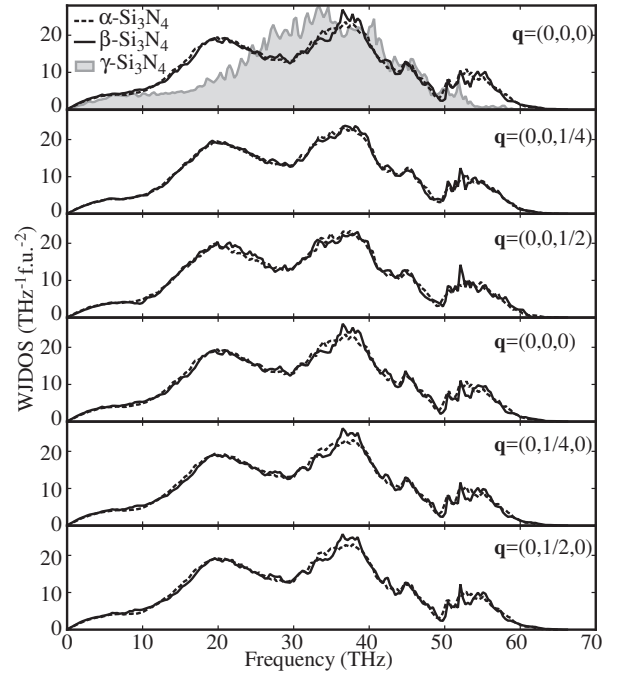


FIG. 5. (color online) WJDOS of  $\alpha$ - and  $\beta$ -Si<sub>3</sub>N<sub>4</sub> at different  $\mathbf{q}$  points and that of  $\gamma$ -Si<sub>3</sub>N<sub>4</sub> at the  $\Gamma$  point. The WJDOS for the  $\alpha$  and  $\beta$  phases in the first and fourth rows are calculated at the same  $\Gamma$ -point but with the polarization for the non-analytic term correction set along  $c^*$  and  $b^*$ , respectively.

two frequency ranges of 0–15 or 0–35 THz for  $\omega_\lambda$  and all indices in  $\lambda'$  and  $\lambda''$ . The frequency ranges for  $\omega_\lambda$  were set so that the narrower frequency range approximately corresponds to the range where the phonon modes largely contribute to  $\kappa$ . A small change in the frequency range by a few terahertz did not change the qualitative characteristics of the averages. To compare the values of the structures with different  $Z$ , we multiply the average by  $(3n_a)^2$  where  $n_a$  is the number of atoms in the primitive unit cell. The averages are very similar for the  $\alpha$  and  $\beta$  phases. With the similar impact of the WJDOS and  $|\Phi_{\lambda\lambda'\lambda''}|^2$ , the phonon lifetimes in these phases are also similar. For the  $\gamma$  phase, the short phonon lifetimes are attributed to the large  $|\Phi_{\lambda\lambda'\lambda''}|^2$  of the low frequency region.

Finally, we examine the striking difference in Fig. 4(d) below  $\sim 5$  THz between the  $\alpha$  and  $\beta$  phases: In the  $\alpha$  phase,  $\tau_{\lambda,\text{ph-ph}}$  below  $\sim 5$  THz are aligned on a single smooth line, while for the  $\beta$  phase, they are scattered roughly on two branches. Fig. 6 enlarges the distributions with two sets of color contrast. In Fig. 6(a), each plot is shown with a color specified by  $\sum_{i,j} \frac{e_j(i,\lambda)q_j}{|\mathbf{q}|}$ , where  $e_j(i,\lambda)$  is the eigenvector component of the  $i$ -th atom's  $j$ -th cartesian coordination. Since  $\sum_{i,j} e_j(i,\lambda)^2 = 1$ , the color contrast indicates the fraction of the eigenvector component along  $\mathbf{q}$ : The brighter (darker) color indicates a larger longitudinal (transverse) component in a phonon mode. In Fig. 6(b), the color contrast is set according to

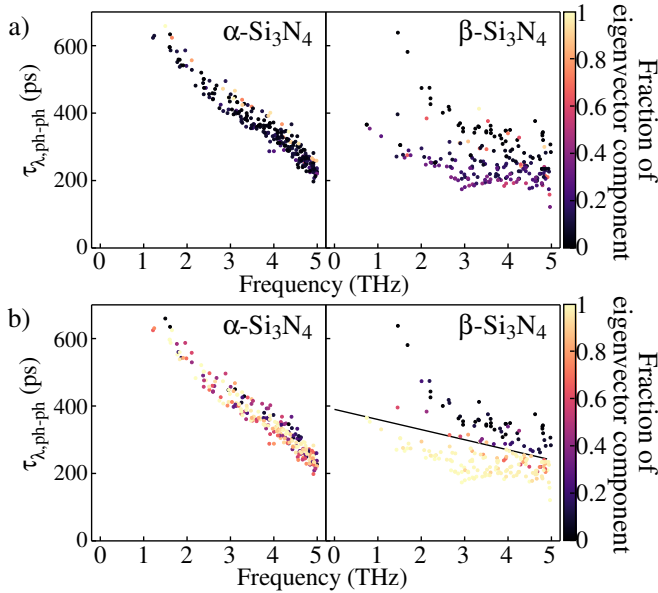


FIG. 6. (color online) Distribution of phonon lifetimes for  $\omega_{\lambda} \leq 5$  THz shown in color with respect to the strengths of the eigenvector components along (a)  $\mathbf{q}$  and (b) on the  $ab$  plane (b).

$\sum_i [e_x(i, \lambda)^2 + e_y(i, \lambda)^2]$ , the fraction of the eigenvector component on the  $ab$  plane.

The colors in Fig. 6(b) show much clearer contrast between the two branches in the  $\beta$  phase than the colors in Fig. 6(a). Therefore, the vibration modes along the  $ab$  plane that belong to the acoustic phonon branches are more easily scattered in the  $\beta$  phase, regardless of how much longitudinal or transverse components they have. For the panel of  $\beta$ -Si<sub>3</sub>N<sub>4</sub> in Fig. 6(b), a straight line splits the phonon modes into two groups. The numbers of the phonon modes assigned to the shorter and longer  $\tau_{\lambda, \text{ph-ph}}$  groups are 145 and 67, of which the ratio is confirmed to be close to the population ratio of the vibration modes along and out of the  $ab$  plane.

#### IV. SUMMARY

In the present study, the lattice thermal conductivities of the three Si<sub>3</sub>N<sub>4</sub> phases were investigated using lattice dynamics based on the first-principles interatomic force constants. The main remarks are as follows:

1) In  $\alpha$ - and  $\beta$ -Si<sub>3</sub>N<sub>4</sub>, of which the crystal structures are characterized by the stacking manner of the basal layer structures,  $\kappa$  is largely altered due to the differences

in the harmonic band structures induced by the different stacking manners. This is in contrast with the zincblende and wurtzite structures in the previous study<sup>15</sup>.  $\kappa$  for  $\alpha$ -Si<sub>3</sub>N<sub>4</sub> is rather isotropic, while  $\kappa_{zz}$  for the  $\beta$  phase is twice or more larger than the other  $\kappa_{ii}$  of the three phases.

2) In the  $\alpha$  phase, the acoustic mode phonons below 6 THz are the main heat carriers, while in the  $\beta$  phase, the phonons below 12 THz contribute to  $\kappa$ . Their group velocities are confirmed to characterize the behavior of  $\kappa$ .

3) In the  $\gamma$  phase, the frequency distribution of the phonon mode contributions to  $\kappa$  is similar to that for  $\kappa_{xx}$  of  $\beta$ -Si<sub>3</sub>N<sub>4</sub>, which is attributed to its large phonon-phonon scattering strength and steep longitudinal acoustic branches.

#### ACKNOWLEDGMENTS

The present work was partly supported by a Grant-in-Aid for Scientific Research (No. 15K14108 from the Ministry of Education, Culture, Sports, Science and Technology (MEXT) Japan and the Elements Strategy Initiative for Structural Materials (ESISM) of Kyoto University.

#### Appendix A: Dependence of the lattice thermal conductivity of $\gamma$ -phase on pressure

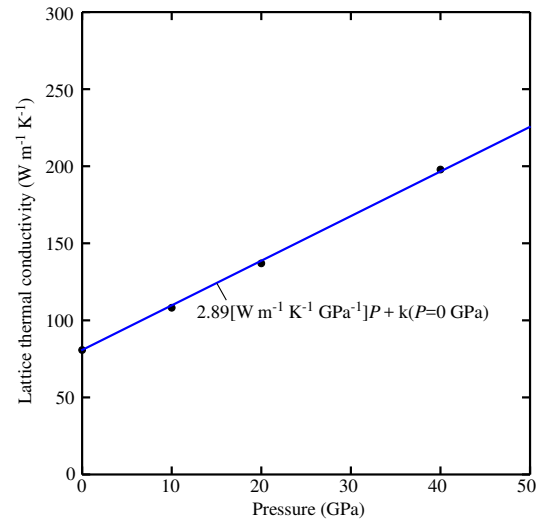


FIG. 7. (color online) Lattice thermal conductivity of  $\gamma$ -Si<sub>3</sub>N<sub>4</sub> as a function of pressure.

\* k-tatsumi@imass.nagoya-u.ac.jp

<sup>1</sup> G. Slack, Journal of Physics and Chemistry of Solids **34**, 321 (1973).



- <sup>2</sup> Y. Zhou, H. Hyuga, D. Kusano, Y.-i. Yoshizawa, and K. Hirao, *Advanced Materials* **23**, 4563 (2011).
- <sup>3</sup> K. Hirao, K. Watari, H. Hayashi, and M. Kitayama, *MRS Bulletin* **26**, 451 (2001).
- <sup>4</sup> K. Watari, *Journal of the Ceramic Society of Japan* **109**, S7 (2001).
- <sup>5</sup> N. Hirosaki, Y. Okamoto, M. Ando, F. Munakata, and Y. Akimune, *Journal of the Ceramic Society of Japan* **104**, 49 (1996).
- <sup>6</sup> N. Hirosaki, S. Ogata, C. Kocer, H. Kitagawa, and Y. Nakamura, *Physical Review B* **65**, 134110 (2002).
- <sup>7</sup> F. L. Riley, *Journal of the American Ceramic Society* **83**, 245 (2000).
- <sup>8</sup> M. Yashima, Y. Ando, and Y. Tabira, *The Journal of Physical Chemistry B* **111**, 3609 (2007).
- <sup>9</sup> D. Du Boulay, N. Ishizawa, T. Atake, V. Streltsov, K. Furuya, and F. Munakata, *Acta Crystallographica Section B: Structural Science* **60**, 388 (2004).
- <sup>10</sup> S. Hampshire, H. Park, D. Thompson, and K. Jack, *Nature* **274**, 880 (1978).
- <sup>11</sup> T. Hahn, ed., *International tables for crystallography*, Vol. A (John Wiley & Sons, Inc., 2011).
- <sup>12</sup> T. Hirai, S. Hayashi, and K. Niihara, *AM. CERAM. SOC. BULL. Am. Ceram. Soc. Bull.* **57**, 1126 (1978).
- <sup>13</sup> B. Li, L. Pottier, J. Roger, D. Fournier, K. Watari, and K. Hirao, *Journal of the european ceramic society* **19**, 1631 (1999).
- <sup>14</sup> R. Vashishta, R. K. Kalia, A. Nakano, and I. Ebbsö, *Amorphous Insulators and Semiconductor*, edited by M. F. Thorpe and M. I. Mitkova (Kluwer, 1996).
- <sup>15</sup> A. Togo, L. Chaput, and I. Tanaka, *Physical Review B* **91**, 094306 (2015).
- <sup>16</sup> A. Zerr, G. Miehe, G. Serghiou, M. Schwarz, E. Kroke, R. Riedel, H. Fueß, P. Kroll, and R. Boehler, *Nature* **400**, 340 (1999).
- <sup>17</sup> Y. Zhang, A. Navrotsky, and T. Sekine, *Journal of materials research* **21**, 41 (2006).
- <sup>18</sup> B. Xu, J. Dong, P. F. McMillan, O. Shebanova, and A. Salamat, *Physical Review B* **84**, 014113 (2011).
- <sup>19</sup> D. Morelli and J. Heremans, *Applied physics letters* **81**, 5126 (2002).
- <sup>20</sup> A. Togo and I. Tanaka, *Scripta Materialia* **108**, 1 (2015).
- <sup>21</sup> L. Chaput, *Physical review letters* **110**, 265506 (2013).
- <sup>22</sup> S.-i. Tamura, *Physical Review B* **27**, 858 (1983).
- <sup>23</sup> P. E. Blöchl, *Phys. Rev. B* **50**, 17953 (1994).
- <sup>24</sup> G. Kresse and J. Furthmüller, *Physical review B* **54**, 11169 (1996).
- <sup>25</sup> G. Kresse, *J. Non-Cryst. Solids* **193**, 222 (1995).
- <sup>26</sup> D. J. Kresse, *Georg. Phys. Rev. B* **59**, 1758 (1999).
- <sup>27</sup> J. P. Perdew, K. Burke, and M. Ernzerhof, *Phys. Rev. Lett.* **77**, 3865 (1996).
- <sup>28</sup> W. Paszkowicz, R. Minikayev, P. Piszora, M. Knapp, C. Bähitz, J. Recio, M. Marques, P. Mori-Sánchez, L. Gerward, and J. Jiang, *Phys. Rev. B* **69**, 052103 (2004).
- <sup>29</sup> D. M. Ceperley and B. Alder, *Physical Review Letters* **45**, 566 (1980).
- <sup>30</sup> S. Wei and M. Chou, *Physical review letters* **69**, 2799 (1992).
- <sup>31</sup> Y. Wang, J. Wang, W. Wang, Z. Mei, S. Shang, L. Chen, and Z. Liu, *J. Phys.: Condens. Matter* **22**, 202201 (2010).
- <sup>32</sup> M. Gajdoš, G. Hummer, G. Kresse, J. Furthmüller, and B. F. F., *Phys. Rev. B* **73**, 045112 (2006).
- <sup>33</sup> X. Wu, D. Vanderbilt, and D. R. Hamann, *Phys. Rev. B* **72**, 035105 (2005).
- <sup>34</sup> M. T. Dove, *Introduction to lattice dynamics*, Vol. 4 (Cambridge university press, 1993) pp. 76–77.
- <sup>35</sup> A. Ward and D. Broido, *Physical Review B* **81**, 085205 (2010).
- <sup>36</sup> R. Minikayev, W. Paszkowicz, P. Piszora, M. Knapp, and C. Bähitz, “Thermal expansion of and silicon nitride,” (2007).
- <sup>37</sup> W. Paszkowicz and R. Minikayev, *Phys. Rev. B* **69**, 052103 (2004).
- <sup>38</sup> P. Andersson, *Journal of Physics C: Solid State Physics* **18**, 3943 (1985).
- <sup>39</sup> A. Cepellotti and N. Marzari, *Physical Review X* **6**, 041013 (2016).
- <sup>40</sup> R. J. Hardy, *Physical Review B* **2**, 1193 (1970).
- <sup>41</sup> S. Mukhopadhyay, L. Lindsay, and D. J. Singh, *Scientific reports* **6** (2016).
- <sup>42</sup> Y. L. Page and P. Saxe, *Phys. Rev. B* **65**, 104104 (2002).
- <sup>43</sup> A. Kuwabara, K. Matsunaga, and I. Tanaka, *Physical Review B* **78**, 064104 (2008).
- <sup>44</sup> L. Lindsay and D. A. Broido, *J. Phys.: Condens. Matter* **20**, 165209 (2008).